ELSEVIER

Biophysical Chemistry 109 (2004) 41–58

Biophysical Chemistry

www.elsevier.com/locate/bpc

Structural dynamics of myoglobin: an infrared kinetic study of ligand migration in mutants YQR and YQRF

Don C. Lamb[a,b], Alessandro Arcovito[c], Karin Nienhaus[a], Oleksandr Minkow[a], Federica Draghi[c], Maurizio Brunori[c], G. Ulrich Nienhaus[a,b,]*

[a]*Department of Biophysics, University of Ulm, D-89069 Ulm, Germany*
[b]*Department of Physics, University of Illinois at Urbana-Champaign, 1110 West Green Street, Urbana, IL 61801, USA*
[c]*Dipartimento di Scienze Biochimiche 'A. Rossi Fanelli', Università di Roma 'La Sapienza', P.le Aldo Moro, 5, 00185 Rome, Italy*

Received 12 September 2003; received in revised form 12 September 2003; accepted 6 October 2003

Abstract

Recombination of carbon monoxide to myoglobin mutants YQR and YQRF was studied using transient infrared absorption spectroscopy and Fourier transform infrared–temperature derivative spectroscopy (FTIR–TDS). Photoproduct states B, C′, C″ and D associated with ligands residing in different protein cavities have been identified. After photolysis, ligands migrate to primary docking site B and subsequently rebind or escape to a secondary site (C) within the Xe4 cavity. For YQR, a global analysis of the isothermal rebinding kinetics below 160 K and the TDS data reveal a correlation between the enthalpy barriers governing the two processes. Above 120 K, a protein conformational change in both YQR and YQRF converts photoproduct C′ into C″ with markedly slowed kinetics. Above ~180 K, ligands migrate to the proximal Xe1 site (D) and also exit into the solvent, from where they rebind in a bimolecular reaction.

Keywords: Protein dynamics; Ligand migration; FTIR spectroscopy; Temperature derivative spectroscopy; Hydrophobic cavities

1. Introduction

Myoglobin (Mb) is a globular protein present in muscle that reversibly binds small ligands [1]. The X-ray structure of sperm whale Mb [2] revealed that there is no open pathway connecting the active site in the interior of the protein to the surrounding solvent. Over the last 40 years, various conjectures have been made concerning possible pathways for ligand migration. Detailed investigations over large ranges in temperature, pH, pressure, viscosity and ionic strength carried out on a wide variety of mutants and different ligands have led to complex reaction schemes and a deeper understanding of protein dynamics [3–11]. Carbon monoxide (CO) has been preferred as a ligand in many studies because of its high nanosecond photolysis quantum yield [12–14] and its relatively strong stretch absorption in the infrared (IR), which allows one to observe the CO in the heme-bound and in the photodissociated states within

---

*Corresponding author. Tel.: +49-731-502-3050; fax: +49-731-502-3059.
E-mail address: uli@uiuc.edu (G.U. Nienhaus).

0301-4622/04/$ - see front matter © 2003 Elsevier B.V. All rights reserved.
doi:10.1016/j.bpc.2003.10.002

the protein [15]. The CO bands are sensitive to electrostatic interactions with the surrounding protein matrix and, therefore, can be used as a marker of ligand location [16,17]. Reorientation, rebinding, CO migration and even CO dynamics within a cavity can be followed directly [17–19].

In the ligand bound state, multiple CO absorption bands are observed due to different protein conformations, referred to as taxonomic or A substates [8,20]. Upon photolysis, the Fe–CO bond is broken and the CO docks in the B state above the heme pyrrole C with its molecular axis parallel to the heme plane [21–23]. From there, CO molecules can migrate to secondary docking sites within internal protein cavities. This process can be induced either by thermal activation or by extended illumination with visible light at low temperatures, where thermal energy is insufficient to overcome the barriers [24,25]. Cryo- and time-resolved crystallographies have led to structural characterization of various photoproduct states [21–23,26–30]. Apart from the primary docking site, CO molecules were also detected in two of the four xenon (Xe) pockets observed by Tilton et al. [31], who measured the crystal structure of metMb under several atmospheres of Xe.

Previously, we have investigated ligand binding in triple mutant YQR with substitutions L29(B10)Y, H64(E7)Q, T67(E10)R and quadruple mutant YQRF with the additional mutation I107(G8)F using Fourier transform infrared–temperature derivative spectroscopy (FTIR–TDS) [18]. Fig. 1 shows essential features of the active site of YQR and YQRF with the CO bound to the heme iron. Additionally, the CO ligand is included at the primary docking site (B), and within the Xe4 (C′) and Xe1 (D) cavities. YQR was initially designed [32] to mimic *Ascaris suum* hemoglobin [33,34]. In our previous work, we were able to distinguish four different intermediates, B, C′, C″ and D, based on the CO spectra and the temperature at which ligand recombination from these intermediates occurred [18]. Here, we complement these results using transient absorption spectroscopy measurements with monitoring in the IR from 12 to 300 K on time scales from 100 ns to 100 s. While FTIR–TDS is a superb method for identifying photoproducts, time-resolved experiments are necessary to obtain the temperature dependence of the dynamics of ligand migration and binding and thus to analyze the energetics of these processes. In this paper, we investigate correlations between structure and enthalpy barrier distributions for mutant YQR by globally fitting the low temperature data from both methods with a single model. In YQRF, ligand rebinding at low temperatures is faster and more heterogeneous than in YQR, due to the presence of the bulky F107 sidechain, and cannot be described by a simple kinetic model. While the interpretation of the spectroscopic and crystallographic data on the intermediate states provides a picture of ligand migration in the protein matrix, the present kinetic analysis allows an estimate of the relevant enthalpy barriers and thus provides the energetics of the migration landscape.

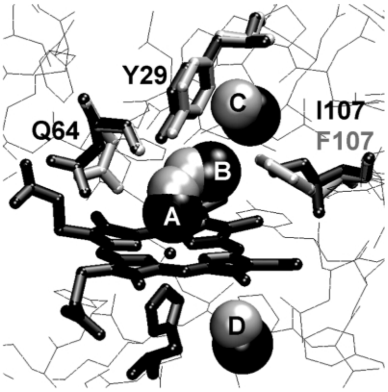

Fig. 1. Structural model of the heme pocket of YQR (mutated residues in dark gray) and YQRF (mutated residues in light gray). The CO is included at various sites: bound to the heme iron (A) [28], at the primary docking site B [22], in the Xe4 cavity (C′) [30] and in Xe1 (D) [30].

2. Materials and methods

2.1. Sample preparation

The YQR and YQRF mutants of sperm whale Mb were expressed in *Escherichia coli* and purified as described previously [32]. The lyophilized protein was dissolved in 75% glycerol/25% potassium phosphate buffer (v/v) (pH 8) at concentrations of 17 and 15 mM for YQR and YQRF, respectively. The sample solutions were stirred for 1 h under one atmosphere of CO. Then, the samples were reduced with twofold excess of sodium dithionite added anaerobically and stirred for another 15 min. Approximately 2 μl of the protein solution were sandwiched between two CaF_2 windows separated by a 75-μm-thick Mylar spacer and mounted in an oxygen-free high conductivity copper sample cell. The Mylar spacer was coated with a thin layer of silicon grease to prevent dehydration of the sample during the measurement. The liquid aliquot did not come in contact with the spacer.

2.2. Infrared transient absorption spectroscopy

Rebinding kinetics data were collected with a home-built transient absorption spectrometer with monitoring in the mid-IR. The instrument consists of a photolysis laser, a monitoring beam and a detection system. The photolysis source is a frequency-doubled Nd:YAG laser (Continuum, Surelite I). The output of the laser was adjusted to 30 mJ per pulse with a pulse width of 6 ns (full-width half-maximum) at a wavelength of 532 nm. The monitoring IR source is a tunable lead-salt diode laser (Laser Photonics, L5622-1932) connected to a closed cycle refrigerator (CTI Cryogenics, compressor S/C 21, cold head M22 DD) and vibration isolation system (Laser Photonics, L5733). The output of the IR laser, tunable over a range of ~100 cm^{-1}, is controlled by a current source (Laser Photonics, 501) and temperature stabilizer (Laser Photonics, 511). The laser emission is collimated by a parabolic mirror with high numerical aperture, focused on the sample, passed through a monochromator, and finally focused on an InSb detector (InfraRed Associates, IS-1). The output was amplified and split between two digitizers. The fast signal (100 ns–300 μs) was recorded using a digital storage oscilloscope (Tektronix, TDS 430A). The second digitizer (Wondertoy II) operates with a logarithmic time base, recording data from 2 μs to 100 s. The instrument control and data collection program was written in LABVIEW (National Instruments). Several kinetic traces were measured at each temperature and averaged. Analysis was performed using software routines written in PVWAVE (Visual Numerics).

The sample cell was masked from both sides using copper tape to ensure that the monitoring beam and photolysis beam impinged on the same sector of the sample. The sample was mounted on the cold finger of a closed cycle refrigerator (CTI Cryogenics) and oriented at 45° with respect to the monitoring beam. It was photolyzed from both sides with the photolysis beam perpendicular to the surface of the windows, due to the high optical density of the sample at 532 nm. The temperature was controlled to within 1 K using a silicon diode (Lakeshore Cryotronics, DT-470 CU13) and temperature controller (Lakeshore Cryotronics, TC-93C).

2.3. Modeling low-temperature rebinding kinetics

Below the glass transition temperature of the cryosolvent (~180 K), global protein motions are frozen out [8]. After photodissociation, ligands cannot escape from the protein; they rebind geminately in a first-order reaction. The kinetics is non-exponential because the protein ensemble is structurally heterogeneous and consists of molecules in different conformational substates, in which CO rebinds with different rates [5]. The simplest scheme to describe the kinetics is a two-well model with bound state A and photoproduct state B and a temperature-independent distribution of enthalpy barriers $g(H)$, which reflects the functional heterogeneity. The fraction of molecules still in the photolyzed state B at time t after the photolysis pulse, $N(t)$, is given by

$$N(t) = \int \mathrm{d}H\, g(H) \exp(-k(H,\ T)t). \tag{1}$$

Frequently, one uses model distributions for $g(H)$, such as a Gaussian, when fitting kinetic data [35],

$$g(H) = \frac{1}{\sqrt{2\pi\sigma^2}} \exp\left(-\frac{(H-H_\mathrm{p})^2}{2\sigma^2}\right), \tag{2}$$

where H_p is the peak enthalpy and σ is the width

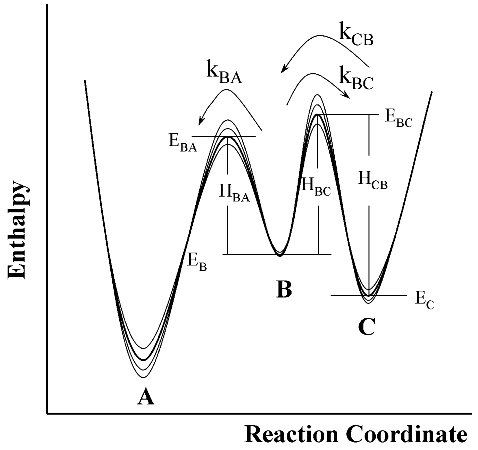

Fig. 2. Rebinding schematic and energy levels of a three-well model describing the dynamics of ligand rebinding in YQR below the dynamical glass transition temperature of the cryosolvent.

of the enthalpy distribution. At temperatures where quantum tunneling can be neglected ($T > 50$ K), the temperature dependence of the rebinding rate coefficient k is described by the Arrhenius relation,

$$k(H,\ T) = A\frac{T}{T_0}\exp\left(-\frac{H}{RT}\right), \tag{3}$$

where A is the attempt frequency, T_0 is a reference temperature (chosen to be 100 K) and R is the gas constant.

In principle, the energy minimum of each well and the enthalpy barriers between wells may be distributed. However, since thermal dissociation is negligible (i.e. $k_{AB} \ll k_{BA}$), the enthalpy distribution in state A can be ignored. Moreover, in the two-well model, the difference in enthalpy between the barrier separating wells A and B and the bottom of well B can be treated as a single enthalpy distribution.

This simplification is no longer feasible if the ligand can migrate to an alternative location C within the protein after photodissociation, which is the case for the mutant proteins in this study. Then it becomes necessary to use a three-well model with distributed energies of wells A, B and C, and the connecting transition states, as shown schematically in Fig. 2. Consequently, a multitude of different reaction surfaces exists. The dynamics is governed by four microscopic rate coefficients, k_{BA}, k_{AB}, k_{BC} and k_{CB}, which are assumed to vary with temperature according to an Arrhenius relation.

The general solution for a sequential three-well model is given below for the following conditions: k_{AB} is negligible and the initial fractional populations of A, B and C are f_A, f_B and $f_C = 1 - f_A - f_B$, respectively:

$$\begin{aligned}
&N(t) = N_B(t) + N_C(t) = 1 - N_A(t),\\
&N_B(t) = \frac{1}{\lambda_1 - \lambda_2}\\
&\quad \times\{(f_B\lambda_1 - (1-f_A)k_{CB})\exp(-\lambda_1 t)\\
&\quad - (f_B\lambda_2 - (1-f_A)k_{CB})\exp(-\lambda_2 t)\}\\
&N_C(t) = \frac{1}{\lambda_1 - \lambda_2}\\
&\quad \times\{(f_B(k_{BA} - \lambda_1) + (1-f_A)(k_{CB} - \lambda_2))\exp(-\lambda_1 t)\\
&\quad - (f_B(k_{BA} - \lambda_2) + (1-f_A)(k_{CB} - \lambda_1))\exp(-\lambda_2 t)\}\\
&\lambda_1 = \frac{(k_{BA} + k_{BC} + k_{CB})}{2}\\
&\quad \times\left(1 + \left[1 - \frac{4k_{BA}k_{CB}}{(k_{BA} + k_{BC} + k_{CB})^2}\right]^{1/2}\right)\\
&\lambda_2 = \frac{(k_{BA} + k_{BC} + k_{CB})}{2}\\
&\quad \times\left(1 - \left[1 - \frac{4k_{BA}k_{CB}}{(k_{BA} + k_{BC} + k_{CB})^2}\right]^{1/2}\right),
\end{aligned} \tag{4}$$

where λ_1 and λ_2 are the apparent, or macroscopic, rate coefficients that are observed experimentally. There are a total of five energy distributions, the distributions in the depths of wells A, B and C, and distributions in the barriers separating the wells (Fig. 2). Again, because thermal dissociation is negligible, the distribution in the depth of well A can be ignored. As our kinetic experiments are only sensitive to energy differences, we can refer all reaction surfaces to one of the four remaining energy levels, for instance, the B or C state, and the reaction surface can be specified by three barrier distributions, $g(H_{BA})$, $g(H_{BC})$ and $g(H_{CB})$.

If the energy barriers are uncorrelated, meaning that the height of each barrier is independent of the height of other barriers, the survival probability $N(t)$ is obtained by integrating over all three distributions:

$$N(t)_{3w}=\iiint \mathrm{d}H_{BA}\mathrm{d}H_{BC}\mathrm{d}H_{CB}g(H_{BA})g(H_{BC})g(H_{CB}) \times[N_B(t)+N_C(t)]. \tag{5}$$

The barriers, however, may be correlated. It is easy to see from Fig. 2 how correlations can arise. If, for instance, the dispersion in enthalpy of well B, $g(E_B)$, is large compared with that of the transition states, $g(E_{BA})$, $g(E_{BC})$, the enthalpy distribution for escape from B to A is given by $g(H_{BA})\approx E_{BA}-g(E_B)$, and the one for escape to C is given by $g(H_{BC})\approx E_{BC}-g(E_B)=g(H_{BA})+\Delta H$, where $\Delta H=E_{BC}-E_{BA}$ is approximately a constant. Hence, the distributions $g(H_{BA})$ and $g(H_{BC})$ are correlated. The opposite case, namely that the distributions in the bottom of wells B and C are small with respect to the distribution in the transition state energies also leads to correlated barriers, with $g(H_{CB})\approx g(E_{BC})-E_C$, $g(H_{BC})\approx g(E_{BC})-E_B=g(H_{CB})-\Delta H'$, where $\Delta H'=E_B-E_C$. Here, there is a linear correlation between enthalpy barrier distributions H_{BC} and H_{CB}. In yet another scenario, the structural determinants that are primarily responsible for the enthalpy barrier between B and A may also govern the enthalpy distribution between B and C. In general, the widths of the distributions may be different. For example, $g(E_{BA})\approx Kg(E_{BC})$, where K is a constant. If K is positive, the barriers are correlated and if K is negative, the barriers are anticorrelated. In the analysis performed here, we fit the data assuming three possible scenarios: a linear correlation between H_{BA} and H_{BC}, a linear correlation between H_{BC} and H_{CB}, and uncorrelated barriers. In the case of correlated barriers, the value of H_{BC} was derived from the correlated enthalpy H_i, with i equal to BA or CB, using the relation

$$H_{BC}=(H-H_i^{p})\frac{\sigma_{BC}}{\sigma_i}+H_{BC}^{p}, \tag{6}$$

where H_i^{p} and σ_i are the peak and width of the Gaussian enthalpy distribution. The ratio of the widths provides the proportionality constant, K. Because of the correlation, one less distribution of protein conformations is needed for calculating $N(t)$, and Eq. (5) reduces to

$$N(t)=\iint \mathrm{d}H_{BA}\mathrm{d}H_{CB}g(H_{BA})g(H_{CB}) \times[N_B(t)+N_C(t)]. \tag{5′}$$

A protein containing two conformations, one where escape to state C is allowed and another one where escape is blocked, can be modeled by a linear combination of the two-well model (Eq. (1)) and a three-well model (Eq. (5)).

2.4. Temperature derivative spectroscopy

To complement the isothermal kinetics measurements, temperature derivative spectroscopy was performed on the identical samples. The sample cell was mounted on the cold-finger of a closed-cycle helium refrigerator (Sumitomo, SRDK-205AW), which allowed regulation of the sample temperature from 3 to 320 K. The sample temperature was measured with a silicon diode and controlled by a temperature controller (Lakeshore Cryotronics, 330). With a Fourier transform IR spectrometer (Bruker, IFS 66v/s), the IR spectra were collected in the mid-IR region between 1800 and 2400 cm^{-1} using an InSb detector at a resolution of 2 cm^{-1}. The sample was photolyzed by a continuous-wave, frequency-doubled Nd:YAG laser (Laser Quantum, Forte 530-300) with 300 mW output at 532 nm. The laser beam was divided with a 50/50 beamsplitter and the sample was irradiated from both sides.

FTIR–TDS is a very powerful method for investigating thermally activated processes involving barrier distributions in proteins [17,18,24,25]. Here, we give only a brief description of the technique. For a more detailed description, we refer the readers to Ref. [36]. In temperature derivative spectroscopy, the sample is perturbed from equilibrium, for instance by photolysis. In the measurements discussed here, we used different illumination protocols to vary the initial condition of the sample before starting the experiment. After photolysis, the temperature of the sample was ramped linearly with time at a warming rate of $\beta = 5$ mK s^{-1}, and transmission spectra were collected every 200 s or 1 K. Consecutive absorption difference spectra were calculated from transmission spectra. FTIR–TDS data are presented as contour plots of the absorbance changes within 1 K on a surface spanned by temperature and wavenumber. Hence, only molecules that have undergone a spectral change between consecutive measurements contribute to a signal in the TDS map. As the relation between temperature and time is linear, the temperature derivative of the population for a first-order process is given by

$$\frac{dN}{dT} = -\frac{N_i}{\beta} k(H, T) \exp(-\Theta), \tag{7}$$

with initial population N_i and resolution function $k(H, T)\exp(-\Theta)$, where

$$\Theta = \int_{T_{\min}}^{T} dT' \frac{k}{\beta}. \tag{8}$$

Here, the rate coefficient $k(H, T)$ is assumed to vary according to the Arrhenius law (Eq. (3)). The temperature at which a process peaks in the TDS contours is approximately proportional to the enthalpy of the process.

For distributed processes, the temperature dependence of rebinding over each enthalpy barrier is multiplied by the probability of a conformational substate having that enthalpy, $g(H)$ (given by Eq. (2)), integrated over all enthalpies:

$$\frac{dN}{dT} = -\frac{N_i}{\beta} \int_0^{\infty} dH\, g(H) k(H, T) \exp(-\Theta). \tag{9}$$

Assuming that the absorption is proportional to the population, dN/dT is proportional to the integral of the absorbances in the FTIR–TDS map calculated across the wavelength region of interest.

For a three-well model, an analytical closed-form solution for dN/dT does not exist. However, dN/dT can be determined numerically. The experiment starts at $T_0 = 3$ K with the ligands distributed between wells B and C. The isothermal three-well model is solved for the first time interval at $T = (T_1 + T_0)/2$ and the populations of N_A, N_B and N_C at T_1 are determined. For the subsequent temperature intervals, N_A, N_B and N_C at temperature T_{i-1} are used as initial populations to calculate N_A, N_B and N_C at T_i. We then calculate N_B and N_C sequentially at each kelvin:

$$\begin{aligned} N_B(T_j) = \sum_{i=1}^{j} \frac{1}{\lambda_1 - \lambda_2} \Big\{ \big[& N_B(T_{i-1})\lambda_1 \\ & - (N_B(T_{i-1}) \\ & + N_C(T_{i-1}))k_{CB}\big] \exp(-\lambda_1 t) \\ & - \big[N_B(T_{i-1})\lambda_2 - (N_B(T_{i-1}) \\ & + N_C(T_{i-1}))k_{CB}\big] \exp(-\lambda_2 t) \Big\} \end{aligned} \tag{10}$$

$$\begin{aligned} N_C(T_j) = \sum_{i=1}^{j} \frac{1}{\lambda_1 - \lambda_2} \Big\{ \big[& N_B(T_{i-1})(k_{BA} - \lambda_1) \\ & - (N_B(T_{i-1}) + N_C(T_{i-1})) \\ & \times (k_{CB} - \lambda_2)\big] \exp(-\lambda_1 t) - \big[N_B(T_{i-1}) \\ & \times (k_{BA} - \lambda_2) - (N_B(T_{i-1}) + N_C(T_{i-1})) \\ & \times (k_{CB} - \lambda_2)\big] \exp(-\lambda_2 t) \Big\} \end{aligned}$$

where $t = (T_i - T_{i-1})/\beta$ or 200 s for 1 K intervals. The fraction of molecules that rebind during each temperature interval, dN_A/dT, is determined from consecutive differences of $N_B(T) + N_C(T)$:

$$\frac{dN_A\big((T_i + T_{i-1})/2\big)}{dT} = -\frac{\big[N_B(T_i) + N_C(T_i)\big] - \big[N_B(T_{i-1}) + N_C(T_{i-1})\big]}{T_i - T_{i-1}}. \tag{11}$$

For distributed barriers, the solution is integrated according to Eq. (5) or according to Eq. (5′) with the appropriate correlations.

2.5. Isothermal kinetics above the dynamical transition temperature

Above the dynamical transition temperature at ~180 K, the protein can undergo global fluctua-

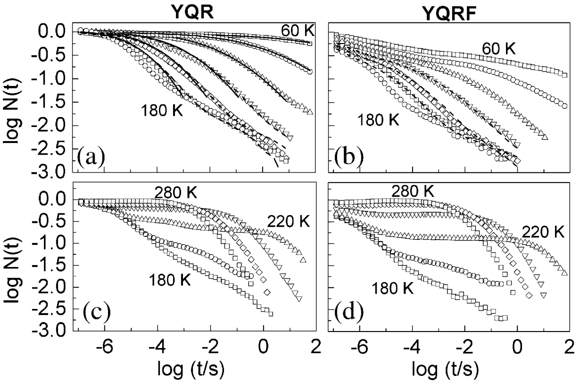

Fig. 3. Isothermal rebinding kinetics of YQR and YQRF (measured in the A_3 substate) in 20 K intervals plotted on a double logarithmic scale. A (B) YQR (YQRF) kinetics from 60 to 180 K and C (D) from 180 to 280 K. The three-well fit for YQR is shown as solid lines. Fits of the C″ state using a three-well model and grouping the internal barriers together are shown as dashed lines in the upper panels.

tions [8,30]. These conformational changes affect ligand migration and rebinding barriers and cause kinetic averaging of the distributions. Therefore, a description of the data with a temperature-independent three-well (or in general multi-well) model with distributed barriers is no longer feasible. Instead, we have calculated the inverse Laplace transform of the rebinding kinetics to obtain the distribution of rate coefficients using the maximum entropy method (MEM) [35]. The MEM finds the most likely distribution that fits the data to the required precision. Temporally well-separated processes are characterized by their average rate coefficients. The temperature dependence of the different processes was analyzed.

3. Results

3.1. Overview of kinetics

Ligand rebinding has been monitored as a function of temperature from 12 to 300 K in the A_3 substates of YQR and YQRF using transient absorption spectroscopy. The photolysis laser power was adjusted such that it provided maximum signal while minimizing laser-heating artifacts. Panels A and B in Fig. 3 show rebinding below the dynamical transition temperature of 180 K. In panels C and D, we plot data taken above 180 K. At lower temperatures, the time traces of YQR and YQRF indicate a very different behavior. In YQR, rebinding between 60 and 120 K appears as a single, distributed process with an enthalpy barrier of 13.4 kJ mol^{-1}. An additional, fast process with 10% amplitude is observed at the lowest temperatures. The overall absorbance change at early times is similar for all kinetic traces. Rebinding speeds up with temperature, and at 140 K a separate, slower process becomes observable on the time scale of 1 s. This process, which will later be assigned to rebinding from the intermediate C″, becomes more pronounced as the temperature is raised to 180 K.

In contrast, YQRF shows two distinct processes. At 60 K, the fast process is observed on times scales below ~1 ms, the slower process extends out to kiloseconds. Approximately 40% of the ligands rebind via the fast process at 60 K. With increasing temperature, these fast-rebinding ligands shift out of the time window of our system, as indicated by the loss of overall absorption at the earliest times. In addition, the fractional contribution of the fast rebinding state increases from 60 to 100 K, implying the availability of both fast and slow rebinding pathways within each molecule. The fast process has a power-law behavior, appearing as a straight line on the double logarithmic plot. The kinetic of the slower process can be described with Eq. (1), using a single, Gaussian-shaped barrier distribution, with a peak enthalpy of 6 kJ mol^{-1}. As in YQR, a slow process (rebinding from C″) becomes observable at 140 K and increases in rate and amplitude as the temperature approaches 180 K.

Above 180 K, the rebinding kinetics of YQR and YQRF are very similar (Fig. 3, lower panels). At 180 and 200 K, fast geminate rebinding is observed at the earliest times and followed by an abrupt change in slope, at which point the ligands have either rebound or escaped to C″. Afterwards, return from C″ is again observed. Above 200 K, the photolyzed ligands can escape to an additional intermediate D and then into the solvent, as indicated by the appearance of a bimolecular rebinding process. The amplitude of the geminate process

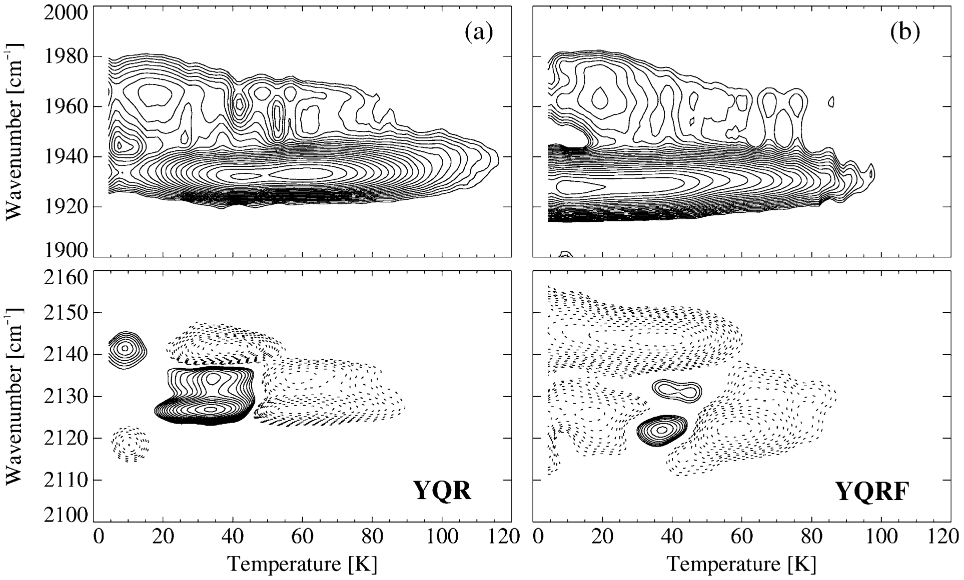

Fig. 4. FTIR–TDS contour maps of (A) YQR and (B) YQRF. The top panels show the absorbance changes in IR bands of heme-bound CO. Absorbance changes of the photoproduct bands are seen in the bottom panels. Contours are spaced logarithmically; solid (dashed) lines represent an absorbance increase (decrease).

decreases substantially between 200 and 240 K. Rebinding rates of the solvent processes in YQR and YQRF are comparable; YQRF rebinds slightly more slowly. In YQRF, the amplitude of the solvent process is smaller than that in YQR.

3.2. TDS experiments after 1-s illumination at 3 K

The kinetics data from the time-resolved IR experiments can be described satisfactorily with a two-well model for YQR and two independent two-well models for the fast and slow processes of YQRF. The FTIR–TDS maps of YQR and YQRF after 1-s illumination at 3 K [18], however, reveal complicated ligand dynamics within the heme pocket that need to be taken into account for a complete analysis of our transient kinetics data. In the TDS data in Fig. 4, positive contours (solid lines) represent an increase in absorbance, whereas negative contours (dotted lines) indicate decaying peak amplitudes.

In the maps of heme-bound CO, two distinct bands are observed, corresponding to discrete protein conformations (taxonomic substates). The dominant band, A_3, is at 1933 cm^{-1} (1929 cm^{-1}) in YQR (YQRF); a minority band A_0 is observable at 1964 cm^{-1} (1963 cm^{-1}). Parameters of Gaussian fits to the A substate bands are given in Table 1. The additional 4 cm^{-1} red shift of A_3 in YQRF with respect to YQR suggests that the F mutation

Table 1
IR stretch frequencies of heme-bound CO in Mb mutants YQR and YQRF at 3 K and Gaussian fits to the bands

Substate	YQR				YQRF			
	Peak position (cm^{-1})	Sigma (cm^{-1})	FWHM (cm^{-1})	Fraction (%)	Peak position (cm^{-1})	Sigma (cm^{-1})	FWHM (cm^{-1})	Fraction (%)
A_0	1964	8	15.7	8	1963	15	8.0	8
A_3	1933	4.1	8.0	92	1929	4.5	8.8	92

changes the protein structure and, concomitantly, the electric field at the binding site.

In YQR, rebinding in the A_0 conformation peaks at 17 K, with an additional long tail extending out to ~90 K. Rebinding in A_3 has maxima at 40 and 60 K. Both A_0 and A_3 exhibit a small fraction that rebinds quickly below 10 K. In the contour map of photodissociated CO (Fig. 4A, lower panel), there are four IR bands at 2119, 2127, 2135 and 2142 cm^{-1}. Below 20 K, the peak at 2119 cm^{-1} (B_2) disappears; and the peak at 2142 cm^{-1} (B_1) increases. In the same temperature region, very little rebinding is visible in the A substate bands, suggesting that the spectroscopic changes in the photoproduct bands reflect rotation of the CO in the primary docking site B, leading to population transfer from B_2 to B_1. This exchange has also been observed in wt Mb [16,17,36]. Above 20 K, B_1 loses population at ~40 K for two reasons: (1) rebinding of CO, as seen by the increase in absorption in the A_3 substate bands, and (2) exchange to a doublet of bands at 2127 and 2135 cm^{-1}, associated with a secondary docking site of the CO, which we call photoproduct site C′ [18]. Above 55 K, B_1 is depleted, and rebinding to A_3 at 60 K occurs from the doublet at 2127 and 2135 cm^{-1}. Photoproduct bands of A_0 are not resolved due to the small fraction in that substate.

In the FTIR–TDS plots of YQRF in Fig. 4B rebinding to the A_0 substate is similar to YQR, peaking at 20 K, and a long tail is observable out to 80 K. The data for A_3, however, deviate significantly from those of YQR. Two rebinding peaks are visible, one near 10 K and a second peak at 30 K. Moreover, a shoulder appears at ~65 K upon closer inspection. In the TDS plot of the photodissociated states, a dominant band is seen at 2144 cm^{-1} together with a myriad of absorption bands below 30 K associated with low temperature rebinding to A_3. Unlike YQR, YQRF does not show the typical B_1/B_2 exchange feature below 20 K, most likely because of the large amount of rebinding. Above 35 K, exchange from the dominant photoproduct band at 2144 cm^{-1} into a doublet at 2123 and 2130 cm^{-1} is visible. This exchange is partially masked by rebinding. Above 60 K, rebinding occurs from the doublet at 2123 and 2130 cm^{-1}. In analogy to YQR, we associate the doublet of bands at 2123 and 2130 cm^{-1} with CO in the photoproduct intermediate state C′.

3.3. Global low-temperature fit

Thermally-induced CO migration from one location to another at 20–50 K (Fig. 4, lower panels) implies that a minimum of three (four) wells are necessary to describe the low-temperature rebinding kinetics of YQR (YQRF). For YQR, we have globally fitted the transient absorption and FTIR–TDS data collected after 1-s illumination with a three-well model (Fig. 5A and B). The temperature derivative of the population, $-\mathrm{d}N/\mathrm{d}T$, was determined by integrating the absorbance difference spectra in the FTIR–TDS contour maps (Fig. 4) along the wavenumber axis, from 1915 to 1950 cm^{-1} for A_3, from 2140 to 2148 cm^{-1} for B_1 and from 2124 to 2135 cm^{-1} for C′. In the global analysis, data points were not taken into account for those times and temperatures where escape to and rebinding from C″ are observable. We note that, after 1-s photolysis, not all ligands are found in B; a small fraction has already escaped to C′ (Fig. 4). The initial subpopulations in B and C′ (82.5 and 17.5%) were estimated by decomposing the 3 K light-over-dark spectrum of photodissociated CO from the FTIR–TDS measurement. Upon photolysis at higher temperatures, e.g. in the isothermal kinetics experiments, we expect more ligands to escape to C′ on very short time scales. Since the remaining ligands in B will preferentially escape to C′ before rebinding from there (Fig. 5C), this uncertainty in the initial population of C′ can be ignored. Fit results are included as lines in Fig. 5A and B; fit parameters are given in Table 2. The errors quoted in the table are standard errors, assuming a normal error distribution and a weak correlation between parameters.

A minimum of four wells is necessary to describe the low-temperature rebinding kinetics of YQRF. All our attempts to fit the YQRF kinetics globally were unsatisfactory. This is due to the complex dynamics in YQRF and the sensitivity of YQRF to light-induced changes in the kinetics, sometimes referred to as ‘pumping’ [24,37]. Our difficulties with YQRF show that a global fit places stringent criteria on the model and parameters used and give us more confidence in our results for YQR.

Table 2
Arrhenius parameters describing the rebinding kinetics in YQR MbCO below 150 K, calculated with a global three-well model

	Log(A/s)	H_1 (kJ mol^{-1})	σ_1 (kJ mol^{-1})
$k_{B_2B_1}$	12[a]	2.4 ± 0.1	1.0 ± 0.1
k_{B*A}	8.6 ± 0.1	7.8 ± 0.9	7.9 ± 0.7
k_{BA}	8.4 ± 0.3	7.9 ± 0.2	1.9 ± 0.1
$k_{BC'}$	10.9 ± 0.3	9.8 ± 0.2	2.4 ± 0.1
$k_{C'B}$	11.7 ± 0.2	16.0 ± 0.2	2.6 ± 0.1

[a] The parameter was fixed during the fitting procedure.

3.4. The C″ state

At 140 K and above, the additional process observed in the kinetic traces is assigned to recombination from yet another intermediate state, C″. To obtain an estimate of the enthalpy barrier distributions governing escape from and rebinding to C″, $g(H_{C'C''})$ and $g(H_{C''C'})$, the rebinding kinetics were fitted from 60 to 160 K. The data points relevant for determination of C″ are in the kinetic traces at 140 and 160 K. In this kinetics calculation, B and C′ were treated as a single state, which is justified, as rebinding from C″ is much slower than rebinding from B or C′. Initially, fits were restricted to those times where the influence of C″ was negligible. After determining the Arrhenius parameters of the internal barrier, $A_{(B/C')A}$ and $H_{(B/C')A}$, with a two-well model, these values were fixed, and the rebinding kinetics were refitted with a three-well model, now including the C″ process. Because of the narrow temperature interval in which C″ could be fit, it was not possible to determine both the pre-exponentials and the enthalpy distribution simultaneously. Hence, the pre-exponentials were fixed at the canonical value of 10^{12} s^{-1} [38,39]. A linear correlation was assumed between $H_{C'C''}$ and $H_{C''C'}$. The calculated kinetics traces are shown as dashed lines in Fig. 3; the fit parameters are compiled in Table 3.

Escape to C″ was not apparent in the FTIR–TDS data in Fig. 4. It is, however, possible to populate C″ in TDS measurements by cooling the

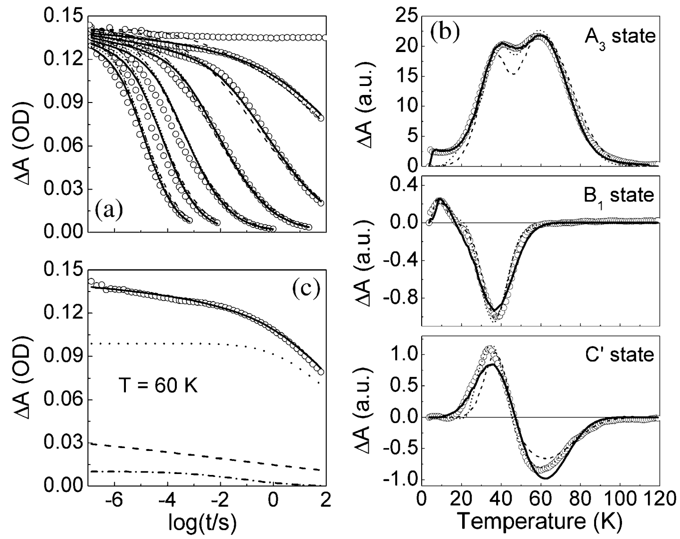

Fig. 5. (A) Isothermal kinetics at 14, 60, 80, 100, 120 and 140 K (from slowest to fastest) for recombination of CO to YQR measured at 1933 cm^{-1}. (B) Integrated absorbance changes calculated across the FTIR–TDS data in Fig. 4, top: A (1920–1950 cm^{-1}); middle: B_1 (2140–2148 cm^{-1}); bottom: C′ (2125–2137 cm^{-1}). Global fits to the data in (A) and (B) were performed assuming a linear correlation between $H_{BC'}$ and H_{BA} (solid line), uncorrelated barriers (dashed line) and a linear correlation between $H_{BC'}$ and $H_{C'B}$ (dotted line). (C) Isothermal rebinding kinetics at 60 K. Components of the fit are included (solid line: total fit; dash-dotted line: rebinding of independent Gaussian, k_{B*A}; dashed line: λ_1; dotted: line, λ_2).

Table 3
Arrhenius parameters describing escape to and rebinding from intermediate C″ in Mb mutants YQR and YQRF

	YQR A_3			YQRF A_3		
	Log(A/s)	H_1 (kJ mol^{-1})	σ_1 (kJ mol^{-1})	Log(A/s)	H_2 (kJ mol^{-1})	σ_2 (kJ mol^{-1})
$k_{\mathrm{C'C''}}$	12[a]	38±4	6±1	12[a]	35±3	5.1±0.8
$k_{\mathrm{C''C'}}$	12[a]	46±3	6±1	12[a]	43±2	5.1±0.8
$k_{\mathrm{C''C'}}$ (TDS)	12[a]	35.4±0.2	4.7±0.2	12[a]	35.9±0.2	5.3±0.2
$k_{\mathrm{C''C'}}$ (MEM)	12[a]	41	–	12[a]	41	–

[a] The parameter was fixed during the fitting procedure.

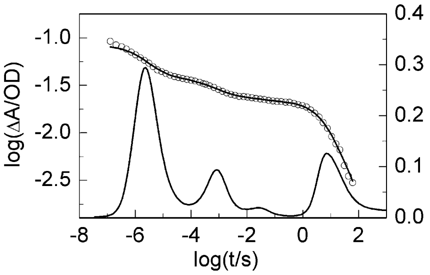

Fig. 6. Isothermal rebinding kinetics (left axis) of YQR at 220 K monitored at 1933 cm^{-1} (shown as open circles). The fit with MEM is shown as a solid line through the data points. The lifetime distribution (right axis) resulting from the MEM analysis is included. The left-most peak arises from escape and rebinding from B/C′, the middle peak from escape and rebinding from C″, and the right most peak from rebinding from solvent.

sample under illumination from 140 to 3 K [18]. The resulting absorbance changes in A_3 were integrated along the wavenumber axis (Fig. 4A and B in Ref. [18]) and fitted with two independent Gaussian distributions. The parameters obtained from this calculation for $k_{\mathrm{C''C'}}$ have been included in Table 3.

3.5. Ligand rebinding above the dynamical transition temperature

Between 180 and 300 K, the rebinding kinetics of YQR and YQRF (Fig. 3, lower panels) are qualitatively similar. When the temperature is increased above 180 K, rebinding from C″ becomes more pronounced. At 190 K, the CO escapes even further away from the binding site to another intermediate state D, as shown by FTIR–TDS [18]. Above 200 K, bimolecular CO recombination from the solvent is observed. Because of protein relaxations and conformational fluctuations, the data in the temperature region from 180 to 290 K were fitted individually to a distribution of lifetimes using the MEM rather than to a temperature-independent distribution of enthalpies. In Fig. 6, we plot the rebinding kinetics of YQR at 220 K as an example, together with the MEM fit to the data and the distribution of lifetimes, which shows three pronounced peaks. The peak at $10^{-5.6}$ s corresponds to rebinding to and escape from C′, the one at $10^{-3.1}$ s is associated with rebinding to and escape from C″, and the peak at $10^{0.9}$ s represents rebinding from the

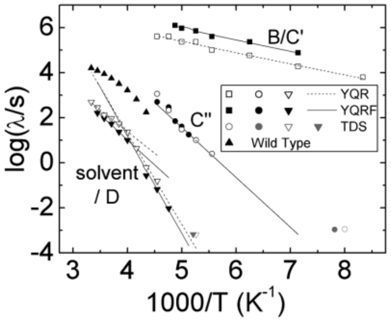

Fig. 7. Arrhenius plot of the apparent rate coefficients determined using MEM: rebinding from B and C′ (□, ■), rebinding from C″ (○, ●) and the solvent process (▿, ▼). Open (closed) symbols represent YQR (YQRF). Rate coefficients determined from TDS experiments are shown in gray. For comparison, the rate coefficients of the solvent process in native sperm whale Mb are included (▲). Dashed lines (solid lines) are fits of the YQR (YQRF) data to the Arrhenius equation (Eq. (3)).

Table 4
Pre-exponentials and enthalpy distributions for the D and S states in Mb mutants YQR and YQRF

	YQR A_3			YQRF A_3		
	Log(A/s)	H_1 (kJ mol^{-1})	σ_1 (kJ mol^{-1})	Log(A/s)	H_2 (kJ mol^{-1})	σ_2 (kJ mol^{-1})
$k_{C''S}$ (MEM)	22	92^b	–	23	95^c	–
$k_{SC''}$ (MEM)	16.7	76^d	–	17.7	81^e	–
$k_{DC''}$ (TDS)	16.7^a	73.4 ± 0.2^f	2.2 ± 0.2	17.7^a	77.7 ± 0.2^g	2.8 ± 0.2

Fits were performed in the temperature intervals [b]220–300 K, [c]210–290 K, [d]180–200 K, [e]195–205 K, [f]160–225 K and [g]160–220 K.

[a] The parameter was fixed during the fitting procedure.

solvent. A small peak at $10^{1.5}$ s cannot be attributed to a particular process at this time. The peak maxima of all lifetime distributions λ are plotted vs. $1000/T$ in Fig. 7. For comparison, the apparent rate coefficients measured in the A_1 substate of wild type sperm whale MbCO at pH 7 are included in Fig. 7.

The apparent rate coefficients λ were fitted to the Arrhenius law (Eq. (3)), yielding an effective enthalpy barrier and attempt frequency. In a three-well model, λ_2 is equal to the rate of return from the third well whenever escape from the middle well to the third one is small [40]. We have estimated $k_{C''C'}$ by fitting λ_2 to an Arrhenius temperature dependence at those temperatures where escape to C″ can be neglected and escape to D is not observed. Because of the narrow temperature interval in which reliable data exist, it was again necessary to fix the pre-exponential to 10^{12} s^{-1} [38,39]. For both YQR and YQRF, the calculated enthalpy barrier $H_{C''C'}$ is identical within error (Table 3). In an analogous fashion, we have estimated the rates of ligand entry from the solvent, taking only the data at those temperatures where little CO escape to the solvent is observed. Parameters are given in Table 4. Below 240 K, a linear fit to the data yields an enthalpy barrier, $H_{S(C''/D)}$, of $\sim$80 kJ mol^{-1}. Above 240 K, the slope of λ_2 changes, and we obtain an effective internal enthalpy barrier for rebinding of 35 and 41 kJ mol^{-1} for YQR and YQRF, respectively. These values are similar to those for rebinding from C″. The enthalpy barrier for escape from C″ to S could be estimated by fitting the rates of ligand rebinding from the solvent to a four-well model, where the previously determined values for $k_{(B/C')A}$, $k_{C'C''}$, $k_{C''C'}$ and $k_{(D/S)C''}$ were fixed. The resulting parameters are given in Table 4.

For comparison, effective rebinding rates were also estimated directly from FTIR–TDS data [36]. A pre-exponential of 10^{12} s^{-1} was used to estimate the kinetics parameters for rebinding from C″ in both YQR and YQRF, and pre-exponentials of $10^{16.7}$ and $10^{17.7}$ s^{-1} obtained from MEM for rebinding from D/S for YQR and YQRF, respectively (Fig. 7, gray symbols).

Rebinding from intermediate D has been studied earlier using FTIR–TDS ([18], Fig. 4). The enthalpy distribution, $g(H_{DC''})$, was determined by integrating the absorbances in the FTIR–TDS maps of bound CO over the entire A state region (1880–1980 cm^{-1} for YQR and 1905–1980 cm^{-1} for YQRF) and fitting the results with Eq. (9). With pre-exponentials taken from the Arrhenius plot (Fig. 7) and assuming a Gaussian $g(H)$ distribution, we obtain kinetic parameters (Table 4) for rebinding from D that are indistinguishable from those describing the solvent process.

4. Discussion

As is evident from both the isothermal kinetics (Fig. 3) and the TDS measurements (Fig. 4), the details of ligand rebinding in YQR and YQRF are markedly different at low temperature, whereas the kinetic traces above 180 K are very similar. Several intermediate states can be distinguished in both YQR and YQRF: state B (the primary docking site in distal heme pocket), state C′, state C″, state D and state S (the solvent).

4.1. Ligand dynamics in the distal heme pocket

The complexity of the CO dynamics within the heme pocket is hidden in the isothermal rebinding kinetics measured in the A_3 absorption band, but clearly observable in the FTIR–TDS map of photodissociated CO (Fig. 4). The isothermal rebinding kinetics of YQR can be fitted with a simple two-well model. This is, however, not in agreement with the FTIR–TDS data, which clearly show rebinding from two distinct CO locations. A reliable fit of the kinetics with a more complex model requires additional information. On the other hand, for the determination of enthalpy barriers from FTIR–TDS data, the attempt frequencies of the processes involved have to be known. Hence, each technique by itself is insufficient for a quantitative description of the dynamics of ligand rebinding. By globally fitting the isothermal kinetics and the FTIR–TDS data, however, we can reliably determine the kinetic parameters of the model and check the validity of more complex kinetic models.

The first dynamic process observed in the FTIR–TDS photoproduct map of YQR (Fig. 4A) is an exchange in population from B_2 to B_1. Anfinrud and coworkers have conjectured from their femtosecond IR studies on wild type Mb at room temperature that B_1 and B_2 are associated with opposite orientations of the CO in the primary docking site B [41]. They suggested that B_2 refers to a CO in state B with the carbon facing towards the heme iron and B_1 to the opposite orientation. Upon photolysis, states B_1 and B_2 are populated according to their accessibilities. They repopulate according to their free energy difference when sufficient thermal energy becomes available. The enthalpy distribution for the exchange, $g(H_{B_1B_2})$, was calculated by fitting the integrated absorbance of B_1 along the wavenumber axis with Eq. (9), assuming a pre-exponential at ~ 10 K of 10^{11} s^{-1} (Table 2) [16]. During the exchange, relatively little rebinding is observed in A_3. The enhancement in population of B_1 is only 15%. Hence, the $B_2 \rightarrow B_1$ exchange will not have a significant impact on the isothermal rebinding kinetics.

A second exchange is observed in the photoproduct map of YQR between 20 and 50 K (Fig. 4). We attribute these features to CO migration from the primary docking site B to a new location C′ for the following reasons: After illuminating the sample at 30 K for 1 h, the majority of ligands populated C′ with photoproduct bands at 2127 and 2135 cm^{-1} (data not shown). The low-temperature photoproduct structure of a YQR MbCO crystal after photolysis at 40 K shows the majority of CO molecules in the Xe4 site [28,42]. Thus, we associate intermediate state C′ with a molecule having CO in the Xe4 cavity. The stretch bands at 2127 and 2135 cm^{-1} represent opposite orientations of the CO at C′; the splitting into two bands arises from different interactions of the CO dipole moment with the internal electric field at the docking site [19,43,44]. The orientation of the CO has essentially no effect on the kinetics, as the temperature dependence of the two bands is identical within experimental error.

To achieve a satisfactory global fit of the YQR data (Fig. 5A and B), it was necessary to include an additional photoproduct state B*. The corresponding kinetic process described by rate coefficient k_{B*A} is shown as a dash-dotted line in Fig. 5C. In general, the process is broadly distributed, showing characteristics similar to recombination to A_0. One possible explanation is an additional conformational substate lying underneath the A_3 band. The existence of spectrally overlapping CO bands related to conformational substates with different structural and kinetic properties has been reported previously for wild type Mb [45]. The additional process $B^* \rightarrow A$ is not well characterized, as seen from the larger error bars in Table 2. The other kinetic parameters are, however, insensitive to the precise values of the Arrhenius parameters.

Fig. 5C shows the rebinding kinetics of YQR at 60 K and the relative contributions of λ_1, λ_2 and k_{B*A}. If $\lambda_1 \gg \lambda_2$, λ_1 corresponds to the escape of ligands from B to either A or C′, whereas λ_2 characterizes rebinding from C′. As seen from the relative amplitudes, the majority of molecules rebind from C′. This explains why the low temperature isothermal kinetics (Fig. 3) can be fitted with a two-well model with bound state A and photolyzed state C′.

The best global fit of the low temperature data was achieved by assuming a positive linear correlation between $H_{BC'}$ and H_{BA}. Fits based on a linear correlation between $H_{BC'}$ and $H_{C'B}$ or uncorrelated barriers were significantly worse (Fig. 5). Additionally, the attempt frequencies for $k_{BC'}$ and $k_{C'B}$, $A_{BC'}$ and $A_{C'B}$, were unphysically high. The enthalpy distribution for rebinding from B, $g(H_{BA})$, agrees within error with results published earlier [18]. The value of 16.0 kJ mol^{-1} for $H_{C'B}$, however, differs from the previously published value of 13.5 kJ mol^{-1} due to the different models used in the analyses [18]. The different attempt frequencies in the independent two-well models and the three-well model analysis account for most of the discrepancy.

The linear correlation between $H_{BC'}$ and H_{BA} can arise from a large distribution in the depth of well B relative to the activation enthalpies for escape from B (Fig. 2) or a structural determinant that influences both transition state enthalpies, E_{BA} and E_{BC}, in a similar fashion. Although a large distribution in B provides a simple explanation, the width of the distribution, 3.2 kJ mol^{-1} full-width half-maximum, may be of the same order as the binding energy of well B. Moreover, if the distribution in E_B were the source of the correlation, we would expect $g(H_{BA})$ and $g(H_{BC'})$ to have similar widths. In a more likely scenario, the Y29 sidechain might influence escape from B to both A and C′. The 3D structure shows tyrosine Y29 in close contact to the CO in state B, and slightly different conformations could lead to correlated distributions.

Elber and Karplus have proposed that access to the Xe4 cavity is gated by residues 68 and 107 [46]. Indeed, in YQRF, F107 protrudes into the distal heme pocket (Fig. 1), pointing towards the primary docking site (B) and hindering ligand escape to remote sites, as verified for photolyzed CO at cryogenic temperatures [18]. The same phenomenon was observed by Ishikawa et al. [47] on human Mb mutants and Scott et al. [10] on a sperm whale mutant having tryptophan at position 107. Its voluminous sidechain was found to destabilize site B, to enhance the amplitude of nanosecond geminate rebinding [48] and to increase the rebinding rate as compared to YQR (this work). The fast rebinders are very susceptible to light-induced changes of the barriers. The many photoproduct bands (Fig. 4) likely arise from CO ligands at a number of additional weak binding sites in the heme pocket that—apart from docking site B—can be populated. Because the fast population rebinds on the submillisecond time scale, the 1-s illumination protocol provides multiple chances for a ligand to find one of these weak binding sites.

4.2. The C″ state

Recombination from intermediate C″ has been characterized based on (i) the 140 K slow cool TDS experiment published previously [18], (ii) isothermal rebinding kinetics at 140 and 160 K and (iii) MEM analysis of the isothermal rebinding kinetics between 180 and 205 K. In YQR and YQRF, rebinding from C″ is kinetically identical within error, but the amplitude of the process is lower in YQRF. This implies that docking site C″ is less accessible in YQRF. The photoproduct spectra of C″ differ considerably for the two mutants (2128 and 2133 cm^{-1} in YQR vs. 2122 and 2128 cm^{-1} in YQRF [18]), indicating that residue 107 is either in close contact with the ligand in C″ or changes the protein structure at C″. In a FTIR–TDS study on a family of Mb mutants, each containing the L29W substitution, the accessibility of the internal cavities was changed by additional mutations [49]. None of the introduced bulky amino acids successfully blocked the C″ site. However, mutations that significantly altered the photoproduct spectra of C″ lined the Xe4 cavity and changed the spectra of C′ as well. This implies that the CO resides in the Xe4 cavity in both C′ and C″.

By analogy, we suggest that a protein relaxation converts photoproduct state C′ into C″, with the ligand remaining in the Xe4 cavity also in YQR(F). Preliminary cryo-crystallographic measurements of the C″ photoproduct structure on YQR MbCO crystals have indeed recovered the ligand in Xe4 (Vallone et al., unpublished). Compared with C′, the sidechain of tyrosine Y29 had moved slightly towards the deoxy position, thus trapping the ligand [42], and the Q64 sidechain had swung deeper into the distal cavity partially occluding the binding site. Because of this steric hindrance, ligand rebinding from C″ is proposed to depend on a concerted conformational motion of the Y29 and Q64 sidechains to reopen access to the active site. Supporting evidence comes from the unusually large and very slow component of geminate NO rebinding in YQR at ambient temperature [42]. The decreased occupancy of C″ (and C′, compare Ref. [18]) in YQRF underscores again the role of F107 as a roadblock against escape to secondary site Xe4.

This relaxation process may explain the discrepancy between the kinetic parameters describing return from C″ (Table 3) determined from FTIR–TDS and isothermal kinetics measurements. The FTIR–TDS measurements are performed below the dynamic glass transition temperature of the protein/solvent, where global motions of the protein are frozen out. A complete relaxation from C′ to C″, however, is expected only above the glass transition temperature. Hence, the value of ~35 $\mathrm{kJ\,mol^{-1}}$ obtained from FTIR–TDS might refer to a partially relaxed protein, whereas the estimate of ~43 $\mathrm{kJ\,mol^{-1}}$ from the isothermal kinetics describes the barrier of a completely relaxed protein.

4.3. Escape to and rebinding from D and S

The nature of intermediate D can be inferred from work on a similar mutant, L29W, for which photoproduct structures have been determined [30]. In state D of L29W, the CO resides in the Xe1 cavity on the proximal side of the heme plane (Fig. 1). Identical CO stretch frequencies (2128 $\mathrm{cm^{-1}}$) in L29W [50] and YQR [18] support the view that the CO ligands also sit in Xe1 in state D of YQR. Further evidence comes from FTIR–TDS studies on wt MbCO crystals [25] and wt MbCO in cryosolvent [51]. They also yielded a photoproduct band at ~2128 $\mathrm{cm^{-1}}$ associated with D. These results are expected if we assume that the local electric field at the proximal site is not affected by the distal mutation.

Upon photolysis above 180 K, ligands can escape to state D and further into the solvent [5]. The rate coefficients for rebinding from the solvent, $k_{\mathrm{SC''}}$, were estimated from the apparent rate coefficients extracted from the MEM analysis in the temperature range between 180 and 240 K. A fit of these data to the Arrhenius relation yielded a barrier $H_{\mathrm{SC''}}$ of ~80 $\mathrm{kJ\,mol^{-1}}$ and a pre-exponential A of ~$10^{17}\ \mathrm{s^{-1}}$. Attempt frequencies larger than 10^{13} may imply temperature dependent enthalpy barrier heights that are not described adequately by the Arrhenius relation. Rebinding from D has been studied earlier by FTIR–TDS measurements under extended illumination ([18], Fig. 4). The enthalpy barrier for rebinding from D, calculated from the TDS data with the pre-exponential obtained from MEM, was identical to that for recombination from S in both YQR and YQRF. Hence, for the measurements reported here, the D and S states are in fast equilibrium; they constitute kinetically a single state (Fig. 7). Consequently, it is irrelevant whether the ligand rebinds from C″ after migration via D or directly from the solvent.

Ligand exit and entry strongly are coupled to the solvent dynamics [52,53]. At ~240 K, a distinct change appears in the slope of the Arrhenius plot of the apparent rate coefficients (Fig. 7). An analogous effect is visible in the wt data (Fig. 7). Below 240 K, less than 50% of all ligands escape into the solvent (Fig. 3). Consequently, the rebinding barrier is lower than the barrier for exit. Ligands reentering from the solvent, will also preferentially bind to the heme iron rather than escape again. The recombination rate is governed by the outer barrier. Above ~240 K, efficient ligand escape after photodissociation indicates that the ligand entry/exit barrier becomes irrelevant compared with the internal barrier that governs the binding process. This raises the question as to which structural features determine recombination. The similar slopes of the data for ligand binding from C″ and D/S in the Arrhenius plot (Fig. 7) suggest that the conformational change that occurs in the C′ to C″ transition governs bimolecular rebinding. The X-ray structure shows that the protein rearranges into the deoxy conformation upon ligand exit from the distal pocket [42], with the sidechains of Y29 and Q64 closing in on the active site. Only rare fluctuations into a deoxy conformation that has a distal pocket structure similar to the A_3 bound-state conformation will allow ligands access to the active site. Consequently, the conformational gate Y29/Q64 governs the bimolecular ligand binding process. A similar mechanism was observed for Mb mutant L29W [50], where the bulky indole group at position 29 gates ligand access to the active site.

4.4. Ligand migration through the protein

YQR and YQRF show essentially a single bound-state conformation A_3 (Table 1), which relaxes, upon ligand escape from the distal pocket, into the deoxy structure [42]. In this conformation, the Y29/Q64 sidechains block access to the primary docking site B, which plays a crucial role in bond formation [41,50]. Moreover, Y29 sequesters the distal pocket into a front half (containing Q64) and a back half (Xe4) and thus prevents migration of ligands from the Xe4 and Xe1 cavities to the front part of the distal pocket. Our kinetic analysis shows that the enthalpy barrier associated with C″ governs bimolecular rebinding. Thus, ligands entering the protein from the solvent will not bind immediately via the primary docking site B, but preferentially migrate to the Xe4 location, as seen from the isothermal kinetics and FTIR–TDS data. There, they are trapped in a protein conformation with blocked access to the active site. For the CO to return to the primary docking site B from intermediate C″, a conformational change is necessary that removes the steric constraints. This process is responsible for the substantial slowing of CO binding compared with wt MbCO (Fig. 7). The much smaller L29 sidechain does not interfere with the docking site.

From these experiments, the nature of the entry and exact pathway(s) of ligands remains obscure. In L29W MbCO, we observed very slow geminate recombination on the time scale of 100 μs [50]. This result was explained by recombination from a secondary site (C, D) in a protein conformation with blocked primary docking site, analogous to the gating scenario invoked here. It implies that ligand migration between secondary sites and solvent is rather inefficient. It appears that other pathways are more important, such as the distal histidine gate, which opens when the imidazole sidechain of H64 swings out of the heme pocket [10].

5. Conclusions

From isothermal kinetic and FTIR–TDS experiments on the YQR and YQRF Mb mutants, we have analyzed the energetics of CO ligand binding and migration among internal cavities. Upon introduction of the large phenyl sidechain at residue 29, photolyzed ligands efficiently escape from the primary docking site B to the Xe4 site C. The additional bulky F107 residue interferes with CO escape at cryogenic temperatures, but has only a minor effect at physiological temperatures. Room temperature measurements of O_2 binding corroborate our observations. The dissociation constants for YQR and YQRF are 1.1 and 0.7 s^{-1}, respectively [48], indicating that the F107 interferes very little with O_2 escape to Xe4 at 20 °C. The distal pocket structures of the ligated and deligated conformations are markedly different. After ligand escape from the active site, Y29/Q64 block access to the primary docking site. This conformational relaxation leads to minimal geminate rebinding of O_2 and CO in YQR at room temperature [42]. The kinetic analysis shows that ligands are trapped in the Xe4 cavity before binding. The rate-limiting step for ligand recombination, however, is the concerted conformational fluctuation of Y29 and Q64 into a more bound-state like distal pocket structure so as to reopen the pathway to the active site. Therefore, both ligand migration and protein motions play crucial roles in the binding reaction of CO to YQR and YQRF Mb.

Acknowledgments

We thank P. Deng for technical assistance and Dr A. Bhattacharyya for helpful discussions. This work was supported by the Deutsche Forschungsgemeinschaft (Ni 291/3) and by the MIUR of Italy (PRIN 2001 on ‘Structural dynamics of heme proteins’).

References

[1] E. Antonini, M. Brunori, Hemoglobin and Myoglobin in their Reactions with Ligands, North-Holland, Amsterdam, 1971.

[2] J.C. Kendrew, R.E. Dickerson, B.E. Strandberg, et al., Structure of myoglobin: a three-dimensional Fourier synthesis at 2 A resolution, Nature 185 (1960) 422–427.

[3] Q.H. Gibson, Hemoproteins, ligands, and quanta, J. Biol. Chem. 264 (1989) 20155–20158.

[4] H. Frauenfelder, N.A. Alberding, A. Ansari, et al., Proteins and pressure, J. Phys. Chem. 94 (1990) 1024–1037.

[5] R.H. Austin, K.W. Beeson, L. Eisenstein, H. Frauenfelder, I.C. Gunsalus, Dynamics of ligand binding to myoglobin, Biochemistry 14 (1975) 5355–5373.

[6] A. Ansari, C.M. Jones, E.R. Henry, J. Hofrichter, W.A. Eaton, Conformational relaxation and ligand binding in myoglobin, Biochemistry 33 (1994) 5128–5145.

[7] P.J. Steinbach, A. Ansari, J. Berendzen, et al., Ligand binding to heme proteins: connection between dynamics and function, Biochemistry 30 (1991) 3988–4001.

[8] J.B. Johnson, D.C. Lamb, H. Frauenfelder, et al., Ligand binding to heme proteins. VI. Interconversion of taxonomic substates in carbonmonoxymyoglobin, Biophys. J. 71 (1996) 1563–1573.

[9] J.S. Olson, G.N. Phillips Jr., Kinetic pathways and barriers for ligand binding to myoglobin, J. Biol. Chem. 271 (1996) 17593–17596.

[10] E.E. Scott, Q.H. Gibson, J.S. Olson, Mapping the pathways for O_2 entry into and exit from myoglobin, J. Biol. Chem. 276 (2001) 5177–5188.

[11] B.A. Springer, S.G. Sligar, J.S. Olson, G. Phillips, Mechanisms of ligand recognition in myoglobin, Chem. Rev. 94 (1994) 699–714.

[12] J.W. Petrich, C. Poyart, J.L. Martin, Photophysics and reactivity of heme proteins: a femtosecond absorption study of hemoglobin, myoglobin, and protoheme, Biochemistry 27 (1988) 4049–4060.

[13] M.R. Chance, S.H. Courtney, M.D. Chavez, M.R. Ondrias, J.M. Friedman, O_2 and CO reactions with heme proteins: quantum yields and geminate recombination on picosecond time scales, Biochemistry 29 (1990) 5537–5545.

[14] J.W. Petrich, J.C. Lambry, K. Kuczera, M. Karplus, C. Poyart, J.L. Martin, Ligand binding and protein relaxation in heme proteins: a room temperature analysis of NO geminate recombination, Biochemistry 30 (1991) 3975–3987.

[15] G.N. Phillips Jr., M.L. Teodoro, T. Li, B. Smith, J.S. Olson, Bound CO is a molecular probe of electrostatic potential in the distal pocket of myoglobin, J. Phys. Chem. B 103 (1999) 8817–8829.

[16] J.O. Alben, D. Beece, S.F. Bowne, et al., Infrared spectroscopy of photodissociated carboxymyoglobin at low temperatures, Proc. Natl. Acad. Sci. USA 79 (1982) 3744–3748.

[17] J.R. Mourant, D.P. Braunstein, K. Chu, et al., Ligand binding to heme proteins: II. Transitions in the heme pocket of myoglobin, Biophys. J. 65 (1993) 1496–1507.

[18] D.C. Lamb, K. Nienhaus, A. Arcovito, et al., Structural dynamics of myoglobin: ligand migration among protein cavities studied by Fourier transform infrared/temperature derivative spectroscopy, J. Biol. Chem. 277 (2002) 11636–11644.

[19] J.M. Kriegl, K. Nienhaus, P. Deng, J. Fuchs, G.U. Nienhaus, Ligand dynamics in a protein internal cavity, Proc. Natl. Acad. Sci. USA 100 (2003) 7069–7074.

[20] H. Frauenfelder, S.G. Sligar, P.G. Wolynes, The energy landscapes and motions of proteins, Science 254 (1991) 1598–1603.

[21] H. Hartmann, S. Zinser, P. Komninos, R.T. Schneider, G.U. Nienhaus, F. Parak, X-ray structure determination of a metastable state of carbonmonoxy myoglobin after photodissociation, Proc. Natl. Acad. Sci. USA 93 (1996) 7013–7016.

[22] I. Schlichting, J. Berendzen, G.N. Phillips Jr., R.M. Sweet, Crystal structure of photolysed carbonmonoxymyoglobin, Nature 371 (1994) 808–812.

[23] T.Y. Teng, V. Srajer, K. Moffat, Photolysis-induced structural changes in single crystals of carbonmonoxy myoglobin at 40 K, Nat. Struct. Biol. 1 (1994) 701–705.

[24] G.U. Nienhaus, J.R. Mourant, K. Chu, H. Frauenfelder, Ligand binding to heme proteins: the effect of light on ligand binding in myoglobin, Biochemistry 33 (1994) 13413–13430.

[25] G.U. Nienhaus, K. Chu, K. Jesse, Structural heterogeneity and ligand binding in carbonmonoxy myoglobin crystals at cryogenic temperatures, Biochemistry 37 (1998) 6819–6823.

[26] V. Srajer, T. Teng, T. Ursby, et al., Photolysis of the carbon monoxide complex of myoglobin: nanosecond time-resolved crystallography, Science 274 (1996) 1726–1729.

[27] V. Srajer, Z. Ren, T.Y. Teng, et al., Protein conformational relaxation and ligand migration in myoglobin: a nanosecond to millisecond molecular movie from time-resolved Laue X-ray diffraction, Biochemistry 40 (2001) 13802–13815.

[28] M. Brunori, B. Vallone, F. Cutruzzola, et al., The role of cavities in protein dynamics: crystal structure of a photolytic intermediate of a mutant myoglobin, Proc. Natl. Acad. Sci. USA 97 (2000) 2058–2063.

[29] K. Chu, J. Vojtchovsky, B.H. McMahon, R.M. Sweet, J. Berendzen, I. Schlichting, Structure of a ligand-binding intermediate in wild-type carbonmonoxy myoglobin, Nature 403 (2000) 921–923.

[30] A. Ostermann, R. Waschipky, F.G. Parak, G.U. Nienhaus, Ligand binding and conformational motions in myoglobin, Nature 404 (2000) 205–208.

[31] R.F. Tilton Jr., I.D. Kuntz Jr., G.A. Petsko, Cavities in proteins: structure of a metmyoglobin–xenon complex solved to 1.9 Å, Biochemistry 23 (1984) 2849–2857.

[32] C. Travaglini Allocatelli, F. Cutruzzola, A. Brancaccio, B. Vallone, M. Brunori, Engineering Ascaris hemoglobin oxygen affinity in sperm whale myoglobin: role of tyrosine B10, FEBS Lett. 352 (1994) 63–66.

[33] J. Yang, A.P. Kloek, D.E. Goldberg, F.S. Mathews, The structure of Ascaris hemoglobin domain I at 2.2 A resolution: molecular features of oxygen avidity, Proc. Natl. Acad. Sci. USA 92 (1995) 4224–4228.

[34] I. De Baere, M.F. Perutz, L. Kiger, M.C. Marden, C. Poyart, Formation of two hydrogen bonds from the globin to the heme-linked oxygen molecule in Ascaris hemoglobin, Proc. Natl. Acad. Sci. USA 91 (1994) 1594–1597.

[35] P.J. Steinbach, K. Chu, H. Frauenfelder, et al., Determination of rate distributions from kinetic experiments, Biophys. J. 61 (1992) 235–245.

[36] J. Berendzen, D. Braunstein, Temperature-derivative spectroscopy: a tool for protein dynamics, Proc. Natl. Acad. Sci. USA 87 (1990) 1–5.

[37] L. Powers, B. Chance, M. Chance, et al., Kinetic, structural, and spectroscopic identification of geminate states of myoglobin: a ligand binding site on the reaction pathway, Biochemistry 26 (1987) 4785–4796.

[38] S. Glasstone, J. Laidler, H. Eyring, The Theory of Rate Processes, McGraw-Hill, New York, 1941.

[39] H. Frauenfelder, P.G. Wolynes, Rate theories and puzzles of heme protein kinetics, Science 229 (1985) 337–345.

[40] W. Doster, D. Beece, S.F. Bowne, et al., Control and pH dependence of ligand binding to heme proteins, Biochemistry 21 (1982) 4831–4939.

[41] M. Lim, T.A. Jackson, P.A. Anfinrud, Ultrafast rotation and trapping of carbon monoxide dissociated from myoglobin, Nat. Struct. Biol. 4 (1997) 209–214.

[42] M. Brunori, F. Cutruzzola, C. Savino, C. Travaglini-Allocatelli, B. Vallone, Q.H. Gibson, Structural dynamics of ligand diffusion in the protein matrix: a study on a new myoglobin mutant Y(B10) Q(E7) R(E10), Biophys. J. 76 (1999) 1259–1269.

[43] E.S. Park, S.G. Boxer, Origins of the sensitivity of molecular vibrations on electric fields: carbonyl and nitrosyl stretches in model compounds and proteins, J. Phys. Chem. 106 (2002) 5800–5806.

[44] S. Franzen, S.G. Boxer, On the origin of heme absorption band shifts and associated protein structural relaxation in myoglobin following flash photolysis, J. Biol. Chem. 272 (1997) 9655–9660.

[45] J.D. Müller, B.H. McMahon, E.Y. Chien, S.G. Sligar, G.U. Nienhaus, Connection between the taxonomic substates and protonation of histidines 64 and 97 in carbonmonoxy myoglobin, Biophys. J. 77 (1999) 1036–1051.

[46] R. Elber, M. Karplus, Enhanced sampling in molecular dynamics: use of the time-dependent Hartree approximation for a simulation of carbon monoxide diffusion through myoglobin, J. Am. Chem. Soc. 112 (1990) 9161–9175.

[47] H. Ishikawa, T. Uchida, S. Takahashi, K. Ishimori, I. Morishima, Ligand migration in human myoglobin: steric effects of isoleucine 107(G8) on O(2) and CO binding, Biophys. J. 80 (2001) 1507–1517.

[48] F. Draghi, A.E. Miele, C. Travaglini-Allocatelli, et al., Controlling ligand binding in myoglobin by mutagenesis, J. Biol. Chem. 277 (2002) 7509–7519.

[49] K. Nienhaus, Ph.D. thesis, University of Ulm, 2003.

[50] K. Nienhaus, P. Deng, J.M. Kriegl, G.U. Nienhaus, Structural dynamics of myoglobin: spectroscopic and structural characterization of ligand docking sites in myoglobin mutant L29W, Biochemistry 42 (2003) 9633–9646.

[51] K. Nienhaus, P. Deng, J.M. Kriegl, G.U. Nienhaus, Structural dynamics of myoglobin: the effect of internal cavities on ligand migration and binding, Biochemistry 42 (2003) 9647–9658.

[52] H. Frauenfelder, P.W. Fenimore, B.H. McMahon, Hydration, slaving and protein function, Biophys. Chem. 98 (2002) 35–48.

[53] P.W. Fenimore, H. Frauenfelder, B.H. McMahon, F.G. Parak, Slaving: solvent fluctuations dominate protein dynamics and functions, Proc. Natl. Acad. Sci. USA 99 (2002) 16047–16051.